ChemElectroChem

Research Article
doi.org/10.1002/celc.202201081

Chemistry Europe
European Chemical Societies Publishing
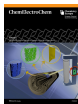
www.chemelectrochem.org

Special Collection

X-Ray Microscopy: A Non-Destructive Multi-Scale Imaging to Study the Inner Workings of Batteries

Flavio Cognigni,*[a] Mauro Pasquali,[a, b] Pier Paolo Prosini,[c] Claudia Paoletti,[c] Annalisa Aurora,[c] Francesca Anna Scaramuzzo,[a] and Marco Rossi[a, b]

X-ray microscopy (XRM) is a non-destructive characterization technique that provides quantitative information regarding the morphology/composition of the specimen and allows to perform multiscale and multimodal 2D/3D experiments exploiting the radiation-matter interactions. XRM is particularly suitable to afford in situ images of inner parts of a battery and for the early diagnosis of its degradation in a non-invasive way. Since traditional characterization techniques (SEM, AFM, XRD) often require the removal of a component from the encapsulated device that may lead to non-desired contamination of the sample, the non-destructive multi-scale potential of XRM represents an important improvement to batteries investigation. In this work, we present the advanced technical features that characterize a sub-micron X-ray microscopy system, its use for the investigation of hidden and internal structures of different types of batteries and to understand their behavior and evolution after many charge/discharge cycles.

Introduction

The COVID-19 crisis revealed the need to enhance resilience through paying attention to new vulnerabilities since entire sectors are undertaking a deep transformation while creating new opportunities to develop Europe's Industry own market, services and production processes to boost its global competitiveness. This must be the opportunity to drive European transitions in a sustainable and fair way and to gear up to become a competitive, resource-efficient, climate-neutral and circular economy by 2050.[1] To support the rapid transition toward electrification, batteries and energy materials research are the key enabling factor to highlight competitiveness and sustainability of a wide range of European Industries operating in diverse sectors such as electronics and semiconductors, e-mobility and stationary energy storage systems.[2] Hence, there is an increasing demand for the development of specific related multi-scale and multi-modal investigation routines and model-based innovation processes covering all stages from materials design to product development, including validation, characterization and life cycle assessment, with the aim of translating innovation challenges into efficient solutions.[1–4] In order to reach a holistic understanding of inner workings of a battery the device must be studied in its assembled state, in its natural physical and chemical environment while potentially performing its function. This is crucial to monitor physical, electrochemical, and micro-to-nano structural changes providing real-time operational information in a correlative microscopy environment. In this context, X-ray microscopy (XRM) can play a pivotal role for early diagnosis of battery degradation in a non-invasive way and represents a driving tool for further correlative microscopy experiments.[5]

[a] Dr. F. Cognigni, Prof. M. Pasquali, Dr. F. A. Scaramuzzo, Prof. M. Rossi
Department of Basic and Applied Sciences for Engineering (SBAI)
University of Rome LA SAPIENZA
Via Antonio Scarpa 14, 00161 Rome (Italy)
E-mail: flavio.cognigni@uniroma1.it
Homepage: https://phd.uniroma1.it/web/FLAVIO-COGNIGNI_nP1714792_IT.aspx

[b] Prof. M. Pasquali, Prof. M. Rossi
Research Center on Nanotechnology Applied to Engineering (CNIS)
University of Rome LA SAPIENZA
Piazzale Aldo Moro 5, 00185 Rome (Italy)

[c] Dr. P. P. Prosini, Dr. C. Paoletti, Dr. A. Aurora
Department of Energy Technologies and Renewable Sources
C.R. ENEA Casaccia
Via Anguillarese 301, 00123 Rome (Italy)

XRM principles and components

X-ray microscopy (XRM) is a non-destructive characterization technique able to provide information on microstructure and phase composition of an object. It offers the possibility to perform multimodal and multiscale 2D/3D experiments[6] employing an experimental set-up that involves three main devices: (a) the source where the X-ray beam formation occurs; (b) the sample stage that is responsible for the mechanical stability of the specimen and allows its rotation during the scan; (b) the detector, typically a flat panel detector (FPD) based on a matrix array fabricated by a complementary metal-oxide semiconductor (CMOS) or a charge-coupled device (CCD), that collects the transmitted X-ray beam. The Beer-Lambert law describes the radiation-matter interaction and highlights an exponential intensity decrease of the X-ray beam when passing through the sample:

$$I(L) = I_0 e^{-\int_0^L \mu(x)dx} \qquad (1)$$

where $I(L)$ indicates the transmitted X-ray beam intensity expressed in Watt, I_0 is the incident X-ray beam intensity expressed in Watt, $\mu(x)$ is the attenuation coefficient value in m^{-1} at the position x expressed in m. Equation (1) is valid when a quasi-monochromatic X-ray beam passing through a heterogenous specimen is considered.[7]

When the X-ray beam impinges into the sample, part of the radiation is absorbed whilst the other portion is transmitted by the object and reaches the detector where it is converted into visible light by a scintillator. The output of the scintillator is magnified and imaged by a camera. This process ensures the acquisition of a single projection image of the sample.[7,8] A set of projections is required to obtain a three-dimensional (3D) reconstruction of the sample; hence the single projection acquisition process is iterated for several rotation angles. After the attainment of an adequate number of projections the reconstruction of the 3D model is assigned to tomographic reconstruction algorithms which are discussed in detail in.[9–11] Laboratory X-ray microscopes generally rely on geometric magnification M that is determined by the Source-Object Distance a (or SOD) and the Object-Image Distance b (or OID):

$$M = (a+b)/a \qquad (2)$$

Modern systems combine geometric magnification, described in Equation (2), with fine focusing optics to reach a sub-micron and nano-scale resolution even when SOD increases.

X-ray experiments can also be run using synchrotron facilities exploiting high-performance features such as high brilliance, monochromatic X-ray beams with excellent directionality and high photon flux to enhance contrast when low density materials are investigated.[12–16] Synchrotron radiation enables high temporal resolution which is crucial for studying dynamic phenomena in complex systems. However, the access to synchrotron facilities is limited and expensive. Therefore, laboratory X-ray microscopes popularity is increasing significantly since they are easier to use and less costly.

XRM techniques for batteries investigation

X-ray characterization techniques are particularly suitable for the investigation of the inner workings of batteries since they are non-destructive and allow multiple length-scales experiments under different conditions. XRM can be used to run ex situ, in situ and in operando experiments in the so-called 4D characterization. In situ and in operando experiments are privileged since batteries can be studied in their chemical and physical environment potentially performing their function.[14,17–22] In order to investigate features at different length-scales and understand many chemical reactions that occur in a battery, different experimental setups and techniques have been developed for XRM. The most common in situ/in operando X-ray characterization techniques are X-ray imaging techniques including Transmission and Scanning X-ray Microscopy (TXM and STXM) and X-ray Computed Tomography (XR-CT); Xray scattering techniques such as X-ray Diffraction (XRD), X-ray Diffraction Computed Tomography (XRD-CT), Energy Dispersive X-ray Diffraction (EDXRD) and X-ray Pair Production Function (XPDF or PDF) and finally X-ray spectroscopy including hard and soft X-ray Absorption Spectroscopy (hXAS and sXAS). In the last decade, the use of XRM investigation techniques for multiscale characterization has rapidly extended becoming widespread as a demonstration of the general interest for in situ/in operando experiments.

In this work we demonstrate the potential of multi-scale in-situ XRM for the investigation of inner working of Na-ion coin cells, Li-ion pouch cells, which were produced exclusively with an aqueous solvent and not organic, and Commercial VARTA NiMH cylindrical cells in their assembled state using an Xradia Versa 610 laboratory microscope from Carl Zeiss Microscopy GmbH. This state-of-art instrument features a dual-stage magnification architecture and a tube that ensures a higher X-ray flux, offering higher contrast-to-noise ratio and remarkable performances at high energy.[23] The image processing and 3D modeling investigation was performed using the software Dragonfly Pro (V. 2022.1) from Object Research Systems (ORS)[24] which demonstrated the capability of reaching a detailed geometric characterization and visualization of single components of the battery from its assembled state. Moreover, the commercial battery was studied at different time-steps after several charge/discharge cycles to monitor the microstructural evolution and defect generation of the device.

Results and Discussion

Na-ion coin cell

X-ray microscopy is a valuable tool for the investigation of coin cell batteries in their assembled state and to verify the accuracy of components positioning during the fabrication process. For this purpose, two replicas of Na-ion battery (cathode material $NaLi_{0.2}Ni_{0.25}Mn_{0.75}O_2$) were characterized via low- and high-resolution experiments. Coin cells' individual components are reported in Figure 1a. Observing 2D slices in the XZ plane of the low-resolution scan (pixel size 27 μm) reconstructed dataset of the first replica it is possible to locate the component's placement after the assembly (see Figure 1b). Three different planes, red, blue and green, were used to get a better visualization of the cathode (red), separator (blue) and the anode material (green) in the ZY plane. These slices were used to verify the correspondence of the actual device internal dimensions with initial parameters and exclude damages occurred during the fabrication processes, as shown in Figure 1b. The metallic components such as the spring, spacer and the underlying copper foil can be clearly distinguished in the three-dimensional representation of the dataset shown in Figure 1c. However, when adjacent materials/phases that compose the sample show remarkable differences in terms of
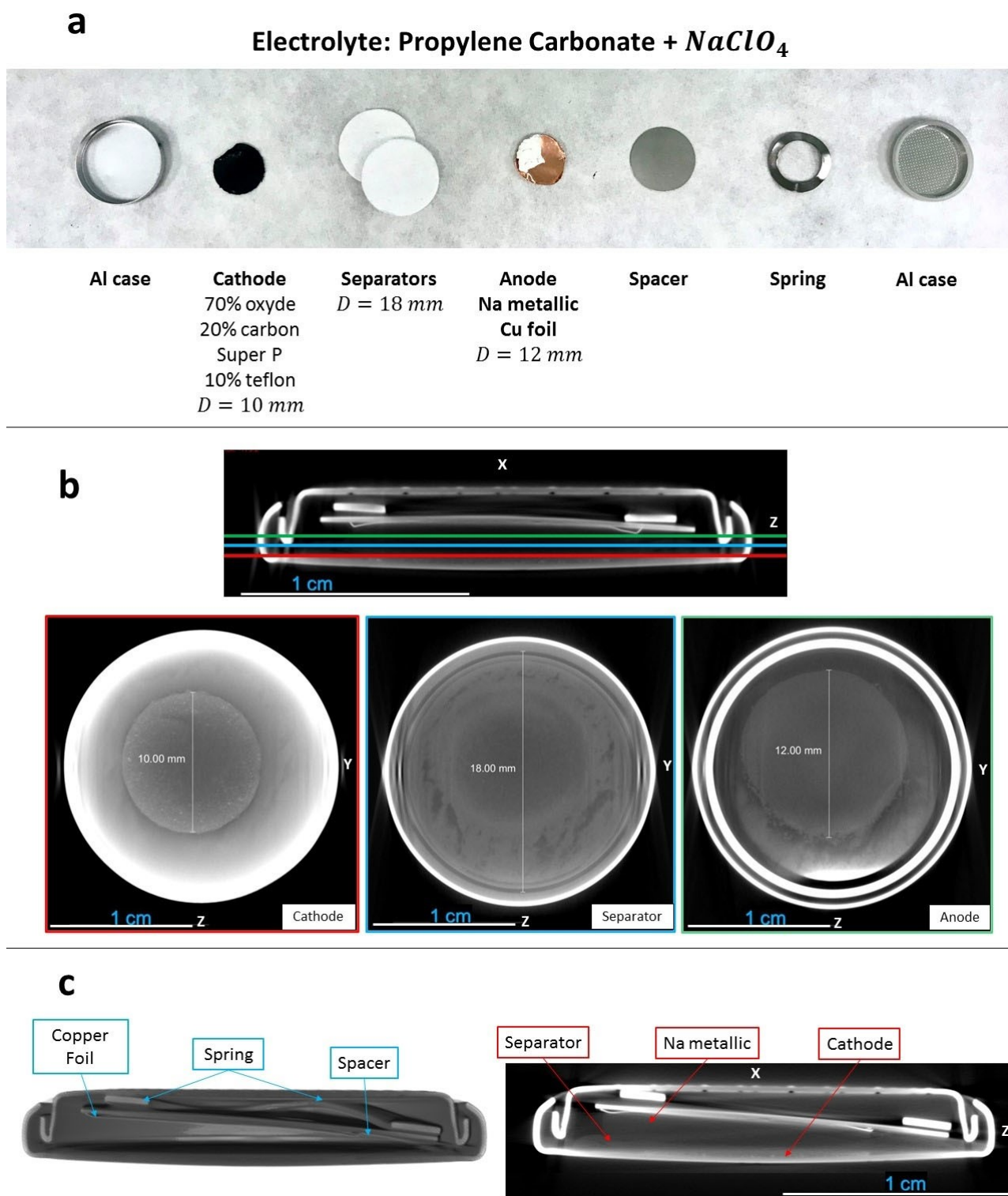
Figure 1. (a) Na-ion coin cell's individual components. (b) 2D cross section in the XZ plane where three planes, red, blue, and green, were used to investigate separately the cathode (red), the separator (blue) and the anode material (green) in the YZ plane. Thus, allowing to verify the correspondence of the actual device internal dimensions with initial parameters and exclude damages occurred during the fabrication processes. (c) 3D representation of the Na-ion coin cell where the metallic components such as the spring, copper foil and spacer are clearly visible. The other parts such as the separator, Na metallic and the cathode material, are represented in the 2D cross section in the XZ plane.

X-ray absorption, such as metal and polymer as in this case, the lighter material is often hidden by the heavier one. For this reason, the brightness/contrast was stressed to make the separator and the metallic Na visible in the digital cross section along the XZ plane, represented in Figure 1c. XRM can also be used to detect critical manufacturing defects that caused the

ChemElectroChem

Research Article
doi.org/10.1002/celc.202201081

Chemistry Europe
European Chemical
Societies Publishing

breakdown of the device. After testing the voltage of the Na-ion coin cell battery second replica, that was null, we analyzed the device via higher resolution imaging (pixel size 12 μm) considering the region of interest (ROI) highlighted by the blue box in Figure 3. This further step offered a clear visualization of a contact zone between the electrodes that originated a short circuit which was investigated in 2D/3D (see Figure 2).
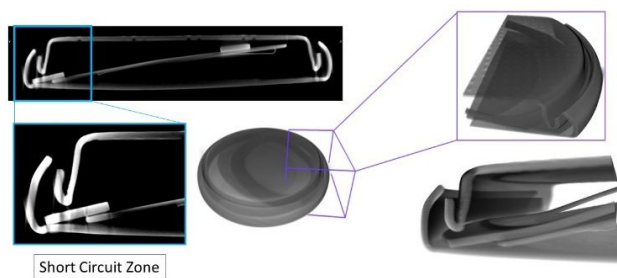

Figure 2. After measuring a null voltage of the Na-ion coin cell battery, multiscale XRM was used to investigate the device slice-by-slice and detect the contact zones between the electrodes. The short circuit, highlighted by the blue box, was characterized in both 2D and 3D.

Li-ion pouch cell

The pouch cell battery (commercial cathode material LiFePO$_4$) was investigated via low resolution scan to provide a general view of the device and guide the placement of the volume of interest (VOI) in the middle of the assembled structure. The selected region was investigated with higher resolution XRM (pixel size 3.7 μm). In this work we considered only the latter scan since the very thin structure of the device cannot be investigated properly with larger pixel size. In Figure 3 a digital cross-section of the pouch cell along the YZ plane is reported. Three-different layers compose the sample. The first one is the cathode, which is in contact with a second layer made of a mixture of glass fibers and electrolyte. The upper layer is the anode made of graphite particles. The average thickness of the device is 390 μm. Each layer was investigated separately in the XY plane. The cathode layer is characterized by the presence of spherical voids, with an average diameter of 15 μm from which multiple cracks originated and evolved through the volume. We believe that during the mixing of the slurry, air bubbles can form as a result of the agitation. Indeed, the intense mixing of
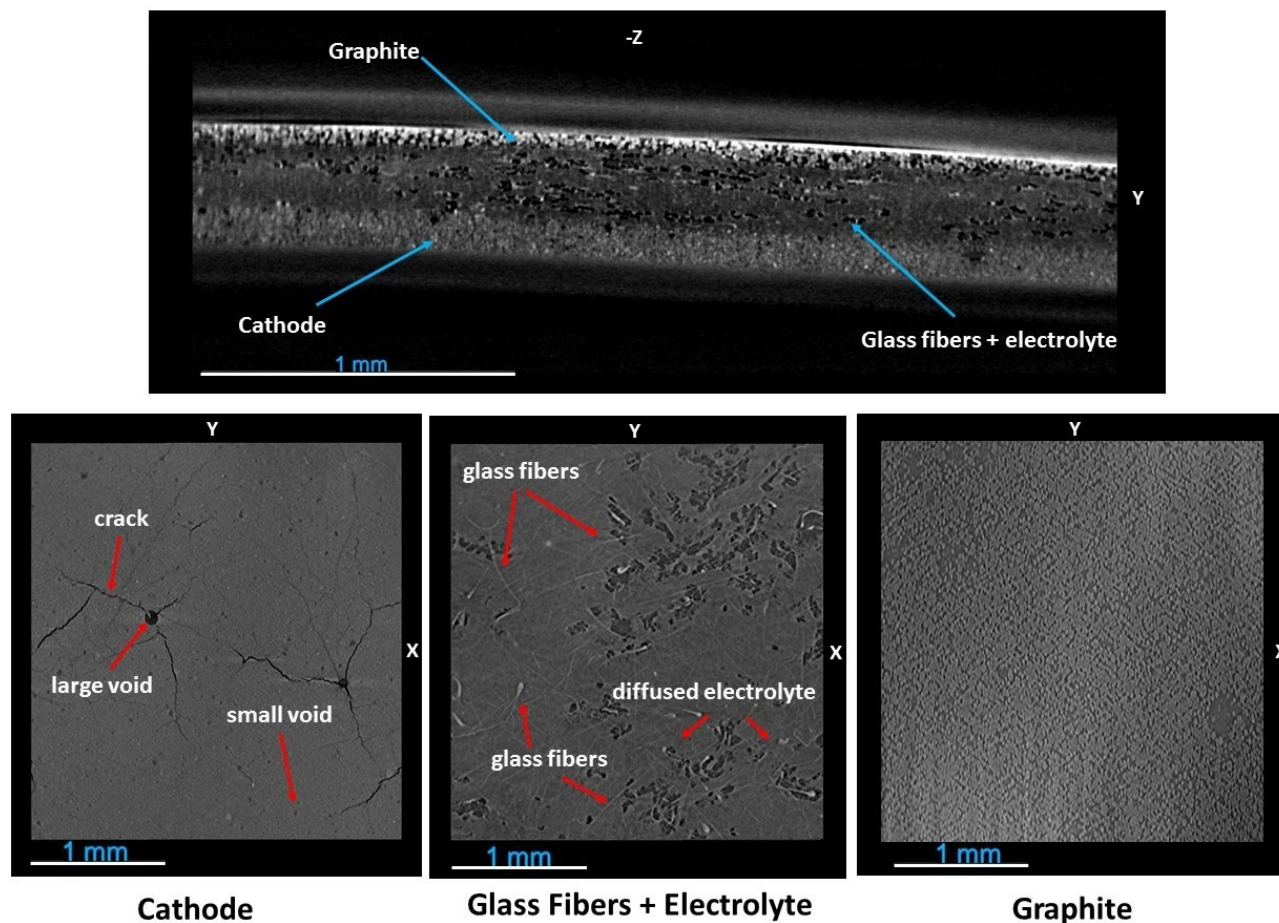

Figure 3. Li-ion pouch cell was investigated via high resolution XRM to provide a digital cross-section of its layered structure in the YZ plane. Three-different layers compose the sample. The first one is the cathode where we highlighted the presence of spherical voids, with an average diameter of 15 μm from which multiple cracks originated and evolved through the volume. During the mixing of the slurry, air bubbles can form as a result of the agitation causing the formation of voids. Then, there is a layer composed of glass fibers dispersed in the electrolyte which probably diffused through the device during the fabrication steps that happened in the high vacuum. The upper one layer is the anode made of graphite particles.

the slurry can introduce air into the mixture, leading to the formation of bubbles.[25,26] During and after the drying process, the small and large spherical voids, caused by the trapped air bubbles, acted as critical regions from which defects such as cracks originated. The second layer shows the presence of glass fibers dispersed in the electrolyte which probably diffused through the device during the fabrication steps that happened in the high vacuum. The upper layer is the anode which is composed of graphite particles with an average diameter of 25 μm.

Commercial VARTA NiMH cylindrical cell

Initial large-scale investigations were performed providing a 3D isotropic voxel size of 54 μm to capture the entire volume of the cell in a single field of view (FOV) and identify large-scales features. Low-resolution XRM showed the general structure of the battery and unlocked helpful information for general orientation in the higher-resolution investigation. The 3D reconstruction shows the inner layers of the electrode assembly revealing the spiral cell architecture, the tap, the electrodes, the separator, and safety devices such as exhaust gas hole and the anti-explosive valve as represented in Figure 4. However, no large-scale bulk defects were located during the inspection of the complex assembly within the cap. The Zeiss Xradia Versa 610 sub-micron XRM system provides the capability to non-destructively (i.e., without sectioning or dismantling) isolate specific ROIs for higher-resolution scans, due to a unique optics-based design. The so-called *Scout & Zoom* procedure[27–29] was employed to probe the inner structure of the battery with a pixel size of 3.6 μm. The arbitrarily selected volume was placed up on the right part of the device as highlighted by the red cylinder in Figure 5. The dataset was processed using a non-local means filter (Kernel size 17, Smoothing 0.5) to remove the noise while preserving the sharpness of strong edges.
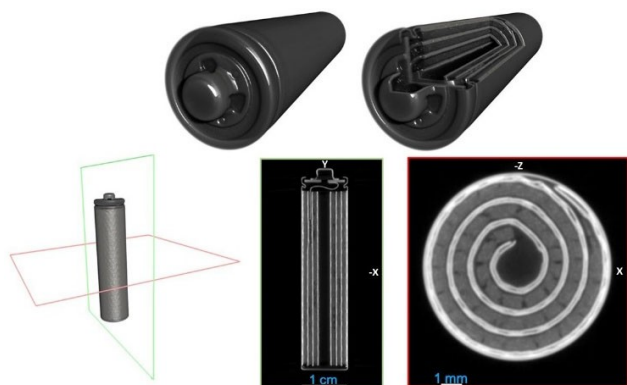

Figure 5. The *Scout-and-Zoom* procedure was employed to probe with higher resolution an arbitrarily selected volume placed up on the right part of the device. This scan provided a detailed view of the inner structure of the battery and allowed the identification of the negative electrode deposited on a nickel foil, the positive electrode, and the nickel foam soaked in it. Since low-energy X-ray were attenuated by the steel casing and the metallic foils it was not possible to distinguish the separator (presumed polymer) from the negative electrode.

This scan provided a detailed view of active layers and allowed the identification and inspection of the negative electrode deposited on a nickel foil, the positive electrode, and the nickel foam soaked in it (see Supporting Information Movie). However, it was not possible to distinguish the separator (presumed polymer) from the negative electrode due to low-energy X-ray absorption by the steel casing and metallic foils. High-resolution XRM was employed to get a three-dimensional investigation of single components. Initially, the negative electrode (yellow), the positive electrode (blue) and the nickel foam (green) were segmented via histogram thresholding. ROIs were refined using process islands functions available in Dragonfly Pro (V. 2022.1). Then, every component was digitally isolated and reported in Figure 6a. This process unlocks the possibility to perform multiple analysis on single components over a wide range of parameters. For instance, the nickel foam local thickness was investigated exporting the labeled pixels into a thickness mesh generating a three-dimensional color map ranging from 15 μm (deep purple) to 80 μm (yellow) as shown in Figure 6b. Observing the thickness distribution histogram a mean value of 35.88 μm and a standard deviation of 7.66 μm was highlighted. The nickel foam geometry revealed a surface-area-to-volume ratio of 113.58 mm^{-1}. High resolution scans allow to study the origin of microstructure defects and monitor their evolution over time as a function of charge/discharge cycling, thermal stresses, and other perturbations that characterize real-world operational condition of the device that may lead to critical failure of the battery.[30–32] Two different replicas of commercial VARTA NiMH cylindrical cell, from the same box, were considered to investigate the origin and the

Figure 4. A low resolution scan was performed to investigate the general structure of a commercial VARTA NiMH cylindrical cell. The 2D/3D representation of the device shows the inner layers of the electrode assembly revealing the spiral cell architecture, the tap, the electrodes, and safety devices such as exhaust gas hole and the anti-explosive valve. These information are crucial for general orientation in the higher-resolution investigation.
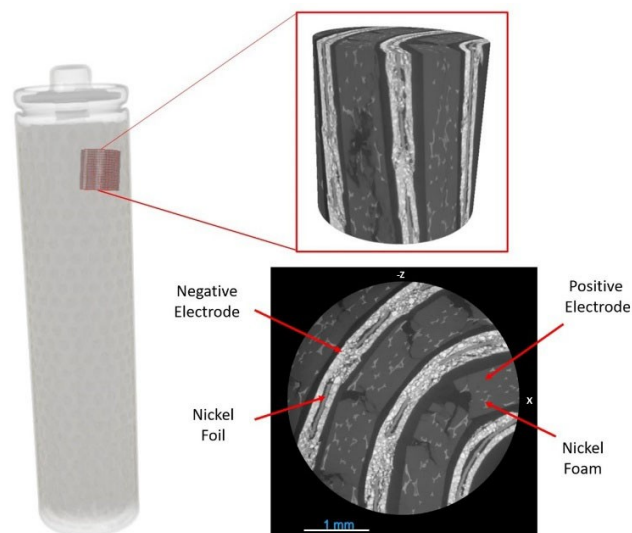
ChemElectroChem

Research Article
doi.org/10.1002/celc.202201081

Chemistry
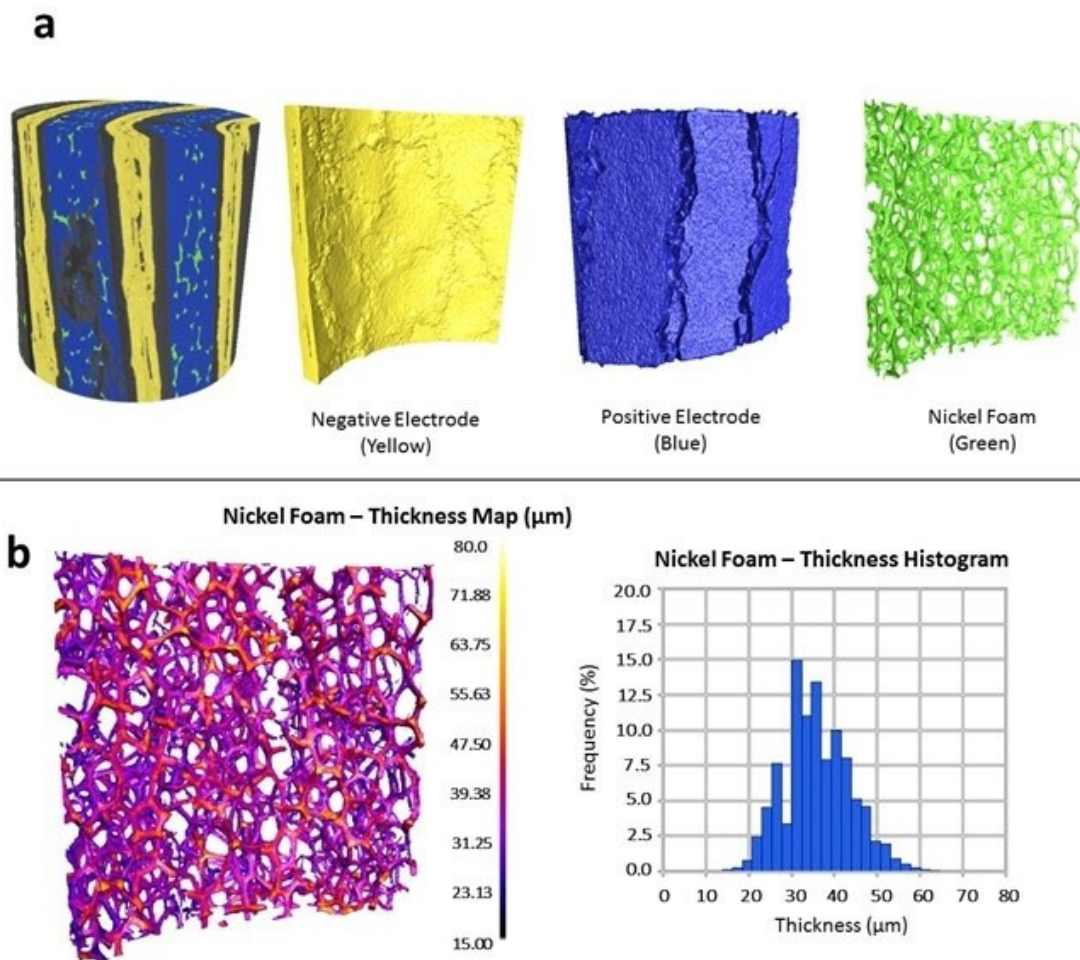Europe
European Chemical
Societies Publishing

Figure 6. (a) High resolution XRM dataset was used to perform multiple analysis on single components. Initially, the negative electrode (yellow), the positive electrode (blue) and the nickel foam (green) were segmented via histogram-based thresholding. Every component was digitally isolated from the device assembly and visualized. (b) For instance, the nickel foam was exported as a thickness mesh to generate a color map ranging from 15 μm (deep purple) to 80 μm (yellow) representing the local thickness of the component. The thickness histogram revealed a mean value of 35.88 μm and a standard deviation of 7.66 μm. The nickel foam geometry revealed a surface-area-to-volume ratio of 113.58 mm^{-1}.

evolution of microstructural defects as function of charge/discharge cycling and capacity fade. The first replica was subjected to a single complete charge/discharge cycle and low- and high-resolution scans were performed at three different states: before cycling (State 1a), at the end of the discharge (State 1b) and after the charge (State 2c). The charge/discharge plot is reported in Supplementary Information as well as some slices of different charge/discharge states. The second replica performed 120 charge/discharge cycles and a capacity fade of 0,011 Ah approximately was detected. The former replica was scanned before and after cycling. These datasets were processed and used to possibly detect the formation of defects in the electrodes, tab or nickel foil and foam. The analysis was conducted performing slice-by-slice investigation to highlight delamination events and cracks formation. Moreover, single components were digitally extracted from their assembled state to monitor eventual variations in terms of volume and surface to be correlated with the capacity fade. The first replica did not show relevant defects related to cycling effects since a

commercial battery is designed and manufactured to undergo thousands of charge/discharge cycles so that capacity fade can be considered null in this specific case. High resolution XRM revealed crucial insights related to the second replica. This device was investigated before and after 120 cycles. The latter scan shows the occurrence of a delamination process and fractures belonging to two different layers of the spiral winding of the device were segmented in green and red for the purpose of visualization. In fact, dynamic volume variations of the negative/positive electrode during the charge/discharge cycles may induce a partial detachment of the active material from the nickel foil and the evolution of cracks that both caused a capacity fade, as in this case (see Figure 7). After many cycles, this phenomenon advances and may determine the failure of the device.
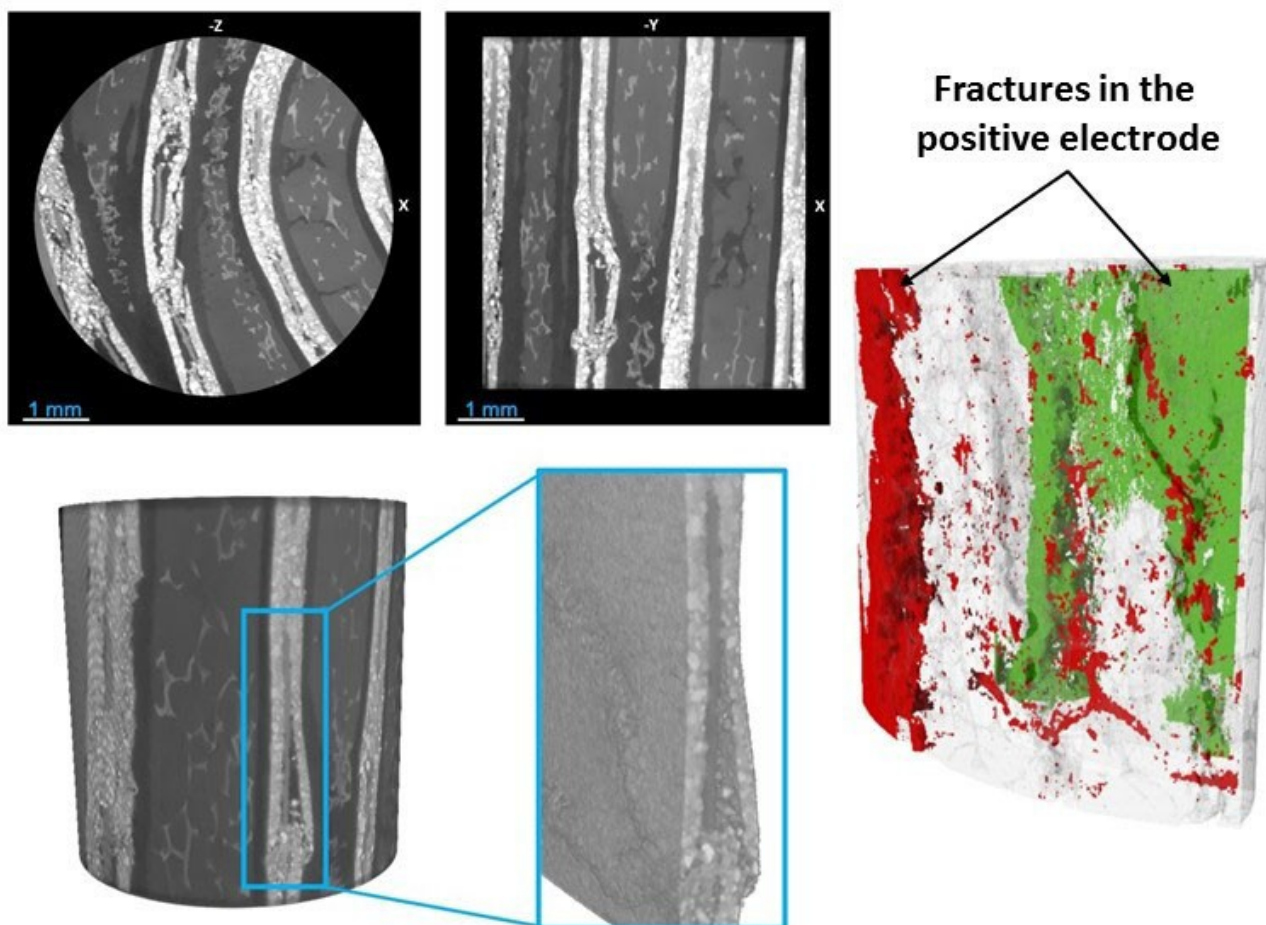
ChemElectroChem

Research Article
doi.org/10.1002/celc.202201081

Chemistry Europe
European Chemical
Societies Publishing

Figure 7. The second replica of a commercial VARTA NiMH cylindrical cell was scanned before and after 120 charge/discharge cycles. High resolution XRM revealed critical insights related to the occurrence of a delamination process. Dynamic volume variations of the negative electrode during the cycling induced a partial detachment of the active material from the nickel foil and the evolution of cracks in the positive electrode that both caused the capacity fade of the device. Fractures belonging to two different layers of the spiral winding of the device were segmented in green and red for the purpose of visualization. The advancement of the process during the battery lifetime may determine the failure of the device.

Conclusion

Multi-scale X-ray microscopy (XRM) was used to perform non-destructive characterization experiments related to Na-ion coin cells, Li-ion pouch cell and a VARTA NiMH cylindrical cells. The devices were initially surveyed with low spatial resolution to investigate the general structure of the battery and any potential large-scale defects. These preliminary results were used to drive the *Scout-and-Scan* procedure and select specific volumes of interest (VOIs). High-resolution XRM revealed internal finer details of the devices within the active layers. We demonstrated the capability to isolate and analyze battery's components separately and extract geometric parameters such as volume, surface, and local thickness. This workflow is a valuable method to study the origin of microstructure defects and the approach can be adopted to monitor their evolution over time as a function of charge/discharge cycling and other perturbations that characterize real-world operational conditions of the device that may lead to critical failure. The commercial VARTA NiMH cylindrical cell was scanned before

and after 120 charge/discharge cycles. High resolution XRM revealed that dynamic volume variations of the negative electrode during the cycling induced a partial detachment of the active material from the nickel foil that caused a capacity fade of the device.

The results of this study highlight the different types of information achievable at each length-scale for several batteries structures and represent a driving tool for further correlative microscopy experiments.

Experimental Section

XRM scan parameters and filtering

Low-resolution Na-ion coin cell. Objective 0.4x, Bin 2, Exposure time 1 s, Source Filter LE6, Voltage 100 kV, Power 14 W, number of projections 1601, pixel size 27.3 μm.

ChemElectroChem

Research Article
doi.org/10.1002/celc.202201081

Chemistry
Europe
European Chemical
Societies Publishing

High-resolution Na-ion coin cell. Objective 0.4x, Bin 2, Exposure time 1 s, Source Filter LE6, Voltage 100 kV, Power 14 W, number of projections 1601, pixel size 12.16 μm.

High-resolution Li-ion pouch cell. Objective 4x, Bin 2, Exposure time 15 s, Source Filter LE2, Voltage 60 kV, Power 6.5 W, number of projections 3201, pixel size 3.74 μm. The dataset was filtered using a gradient-domain diffusion filter (XY Sigma 5; Z Sigma 4; Weight 0.08) and an horizontal destriping filter (Sigma foreground and background 128 pixels; Level 5, Wavelet db18).

Low-resolution commercial VARTA NiMH cylindrical cell. Objective 0.4x, Bin 2, Exposure time 2 s, Source Filter HE4, Voltage 160 kV, Power 25 W, number of projections 1601, pixel size 52.53 μm.

High-resolution commercial VARTA NiMH cylindrical cell. Objective 4x, Bin 2, Exposure time 8 s, Source Filter HE6, Voltage 160 kV, Power 25 W, number of projections 3201, pixel size 3.62 μm. The dataset was processed using a non-local means filter (Kernel size 17, Smoothing 0.5).

Batteries characteristics

Li-ion pouch cell. The electrodes were realized by deposition and drying of a suspension realized with a powdered mixture in water. Triton X-100 (*t*-Octylphenoxypolyethoxyethanol, Polyethylene glycol *tert*-octylphenyl ether, Sigma-Aldrich) was used as a non-ionic surfactant. Carbon Black [Super P, MMM Carbon, Brussels, Belgium] was used to increase the electric conductivity. The cathode active material was commercial $LiFePO_4$ [Linyi-Gelon company (Linyi, ShanDong, GuangDong, China] while the anode active material was commercial graphite (Linyi, ShanDong, GuangDong, China). Sodium carboxymethyl cellulose (Na–CMC, $M_w \sim 90,000$, Sigma-Aldrich) was used as binder. To prepare the electrode the powdered components were mixed in the percentage as indicated in Table 1 for about 10 minutes and then passed through a 250 mm sieve.

The powder mixture is then further mixed for about 2 hours in a jar with glass spheres. The slurry was prepared by mixing the powder mixture containing the active materials and the additives with water. The aqueous suspension was deposited on a metallic current collector through the doctor blade technique. An aluminum foil was used for the cathode and a copper one for the anode. The thickness of the foils was 20 mm. The cathode tapes were made by setting the height of the blade at 330 mm. The anodes have been made with the doctor blade at a height ranging from 70 to 100 mm. The tapes were initially left to dry in air at room temperature and then in a dry room at 20 °C for at least 24 hours. After drying, the electrode tapes were compressed through two stain steel rollers to reduce the height at about 90 % of the initial one. The final thickness of the electrodes was about 100 mm for the cathode and 50 mm for the anode. Rectangular electrodes of about 26 cm^2 were cut from the tape. An aluminum tab was sealed to the cathode and a nickel tab to the anode. As separator was used a glass microfiber filter (Grade GF/A, Whatman). The electrodes and the separator were housed inside a plastic/metal laminate fold (polyester/aluminum/polyethylene). The electrolyte (lithium

hexafluorophosphate solution in ethylene carbonate and dimethyl carbonate, 1.0 M $LiPF_6$ in EC/DMC = 50/50 (*v/v*), battery grade, Sigma-Aldrich) was inserted into the cell just before sealing the last side of the pouch cell under vacuum. The electrochemical test was carried out at C/20 between 3.55 V for charging and 2.0 V for discharging.

Na-ion coin cells. The cathode material of formula $NaLi_{0.2}Ni_{0.25}Mn_{0.75}O_\delta$ was synthesized by means of a variant of the acetate method proposed by Prosini et al. [P.P. Prosini, M. Carewska, C. Cento, G. Tarquini, F. Maroni, A. Birrozzi, F. Nobili. Tin-decorated reduced graphene oxide and $NaLi_{0.2}Ni_{0.25}Mn_{0.75}O_\delta$ as electrode materials for sodium-ion batteries. Materials, 12, 2019, 1074]. Briefly, 2.720 g of sodium acetate trihydrate (ACS reagent, ≥99 %, Sigma-Aldrich), 0.408 g of lithium acetate dihydrate (for synthesis 99 %, Sigma-Aldrich), 1.244 g of nickel (II) acetate tetrahydrate (98 %, Sigma-Aldrich) and 3.676 g of manganese (II) acetate tetrahydrate (for synthesis 99 %, Sigma-Aldrich) are placed in a beaker and dissolved in 4 ml of water. The solution is warmed under stirring at T > 100 °C to allow the water to evaporate. The forming gel is transferred to a ceramic crucible for the subsequent thermal treatment which involves a ramp temperature rate of 0.5 °C/min up to 850 °C and then a dwell step for 4 h. Cooling to room temperature was carried out with an 8 °C/min temperature rate. The composite cathode tape was made by calendaring a mixture of 0.400 of active material, 0.043 g of binder (Teflon, DuPont, Midland, MI, USA) and 0.091 g of carbon (Super P, MMM Carbon, Brussels, Belgium). The composition of the electrode tape was 70.0 wt% active material, 10.0 wt% Teflon and 20.0 wt% Super P carbon. From the tape were punched circular electrodes with a diameter of 12 mm. The electrodes were tested in a two-electrode sodium cell in which the sodium served as both the counter and the reference electrode. The cells were assembled placing two Whatman glass microfiber disks (Grade GF/A), used as a separator, between the positive and the negative electrode. In Figure 1a are shown all the individual components of a coin cell before the assembling. A 1.0 M solution of $NaClO_4$ dissolved in propylene carbonate was used as the electrolyte.

Commercial VARTA NiMH cylindrical cell. A commercial NiMH battery was used (AAA 800 mAh 1.2 V HR03 Micro 56703 ACCU, Varta). The electrochemical test was carried out at C/2 between 4.10 V for charging and 2.30 V for discharging.

Cycling test. The cycling tests were automatically carried out either with a battery cycler (Maccor 4000) or a potentiostat/galvanostat EC-Lab V6.92 (VARTA NiMH cylindrical cell Replica 1). All experimental activities were performed at 20 °C in a dry room (R.H. < 0.1 % at 20 °C).

Table 1. Percentage of the components in the cathode and in the anode.

Component	Cathode [%]	Anode [%]
$LiFePO_4$	85.0	–
Graphite	–	95.5
Super P	9.4	1.9
Na–CMC	3.7	2.6
Triton X-100	1.9	–

Conflict of Interest

The authors declare no conflict of interest.

Data Availability Statement

The data that support the findings of this study are available from the corresponding author upon reasonable request.

[1] European Commission, "Horizon Work Program 2023–2024", can be found under: https://ricerca.unicatt.it/ricerca-wp-7-digital-industry-and-space_horizon-2023-2024_en.pdf, 2019 (accessed 4 December 2022).

[2] European Commission – Batteries Europe, "Strategic Research Agenda for batteries 2020" can be found under: https://digital-strategy.ec.europa.eu/en/news/batteries-europes-strategic-research-agenda-sets-priorities-future-battery-research, 2020 (accessed 2 June 2022).

[3] European Commission, "Horizon Europe – Work Programme 2021–2022", can be found under: https://ec.europa.eu/info/funding-tenders/opportunities/docs/2021-2027/horizon/wp-call/2021-2022/wp-1-general-introduction_horizon-2021-2022_en.pdf, 2022 (accessed 2 June 2022).

[4] Italian Parliament, "Il Piano Nazionale di Ripresa e Resilienza (PNRR)", can be found under: https://www.governo.it/sites/governo.it/files/PNRR.pdf, 2021 (accessed 2 June 2022).

[5] D. Dini, F. Cognigni, D. Passeri, F. A. Scaramuzzo, M. Pasquali, M. Rossi, *J. Electrochem. Soc.* 2021, *168*, 126522.

[6] K. E. Duncan, K. J. Czymmek, N. Jiang, A. C. Thies, C. N. Topp, *Plant Physiol.* 2022, *188*, 831–845.

[7] Eds. S. Carmignato, W. Dewulf, R. Leach in *Industrial X-Ray Computed Tomography*, Springer Cham, 2018.

[8] J. Hsieh in *Computed Tomography: Principles, Design, Artifacts, and Recent Advances*, SPIE PRESS BOOK, 2003.

[9] G. Wang, J. C. Ye, K. Mueller, J. A. Fessler, *IEEE Trans. Med. Imaging* 2018, *37*, 1289–1296.

[10] G. Wang, J. C. Ye, B. De Man, *Nat. Mach. Intell.* 2020, *2*, 737–748.

[11] S. R. Stock in *MicroComputed Tomography: Methodology and Applications*, CRC Press, 2020.

[12] L. Feng, L. Yijin, Y. Xiqian, *Chem. Rev.* 2017, *117*, 13123–13186.

[13] Z. Gong, Y. Yang, *J. Energy Chem.* 2018, *27*, 1566–1583.

[14] J. B. Leriche, S. Hamelet, J. M. M. Shu, C. Masquelier, G. Ouvrad, M. Zerrouki, P. Soudan, S. Belin, E. Elkaim, F. Baudelet, *J. Electrochem. Soc.* 2010, *157* A606.

[15] K.-W. Nam, S.-M. Bak, E. Hu, X. Z. Y. Yu, X. Wang, L. Wu, Y. Zhu, K.-Y. Chung, X.-Q. Yang, *Adv. Funct. Mater.* 2013, *23*, 1047–1063.

[16] M. B. Dixit, A. Verma, W. Zaman, X. Zhong, P. Kenesei, J. S. Park, J. Almer, P. P. Mukherjee, K. B. Hatzell, *Appl. Energy Mater.* 2020, *3*, 9534–9542.

[17] J.-H. Cheng, A. A. Assegie, C.-J. Huang, *J. Phys. Chem.* 2017, *121*, 7761–7766.

[18] J. Nelson, S. Misra, Y. Yang, A. Jackson, Y. Liu, H. Wang, H. Dai, J. C. Andrews, Y. Cui, M. F. Toney, *J. Am. Chem. Soc.* 2012, *134*, 6337–6343.

[19] X. Yan, Y. Yifan, Z. Shuyang, *Nano Lett.* 2019, *19*, 2928–2934.

[20] S.-C. Chao, Y.-C. Yen, Y.-F. Song, Y.-M. Chen, H.-C. Wu, N.-L. Wu, *Electrochem. Commun.* 2010, *12*, 234–237.

[21] N. A. Canas, S. Wolf, N. Wagner, A. K. Friedrich, *J. Power Sources* 2013, *226*, 313–319.

[22] W. Li, M. Li, Y. Hu, J. Lu, A. Lushington, R. Li, T. Wu, T.-K. Sham, X. Sun, *Small Methods* 2018, *2*, 8.

[23] Carl Zeiss Microscopy GmbH, "ZEISS Xradia Versa X-ray Microscopes", can be founder under: https://www.zeiss.com/microscopy/en/products/x-ray-microscopy/xradia-versa.html 2022 (accessed 12 September 2022).

[24] Object Research Systems (ORS) Inc., "Dragonfly is the Premier Software Platform for Scientific Image Processing", can be found under https://theobjects.com/index.html, 2022 (accessed 16 September 2022).

[25] M. Schmitt, M. Baunach, L. Wengeler, K. Peters, P. Junges, P. Scharfer, W. Schabel, *Chem. Eng. Process.* 2013, *68*, 32–37.

[26] W. B. Hawley, J. Li, *J. Energy Storage* 2019, *25*, 100862.

[27] A. P. Merkle, J. Gelb, *Microsc. Today* 2013, *21*, 2.

[28] M. Feser, J. Gelb, H. Chang, H. Cui, F. Duewer, S. H. LAU, A. Tkachuk, W. Yun, *Meas. Sci. Technol.* 2008, *19*, 9.

[29] T. L. Burnett, S. A. McDonald, A. Gholinia, R. Geurts, M. Janus, T. Slater, S. J. Haigh, C. Ornek, F. Almuaili, D. L. Engelberg, G. E. Thompson, P. J. Wither, *Sci. Rep.* 2014, *4*, 4711.

[30] D. Belov, M.-H. Yang, *J. Solid State Electrochem.* 2008, *12*, 885–894.

[31] D. Lu, Y. S. Shao, T. Lozano, W. D. Bennett, G. L. Graff, B. Polzin, J. Zhang, M. H. Engelhard, N. T. Saenz, W. A. Henderson, P. Bhattacharya, J. Liu, J. Xiao, *Adv. Energy Mater.* 2014, *5*, 3.

[32] Q. Wang, B. Mao, S. I. Stoliarov, J. Sun, *Prog. Energy Combust. Sci.* 2019, *73*, 95–131.

[33] T. Hosaka, K. Kubota, H. A. Shahul, *Chem. Rev.* 2020, *120*, 6358–6466.